



Graphene oxide/cobalt-based nanohybrid electrodes for robust hydrogen generation



Fabiola Navarro-Pardo^{a,b}, Xin Tong^{b,c}, Xin Tong^{a,b}, Gurpreet S. Selopal^{a,b}, Sylvain G. Cloutier^d, Shuhui Sun^b, Ana C. Tavares^b, Haiguang Zhao^{e,**}, Zhiming M. Wang^{a,*}, Federico Rosei^{a,b,*}

^a Institute of Fundamental and Frontier Sciences, University of Electronic Science and Technology of China, Chengdu, 610054, P.R. China

^b Center for Energy, Materials and Telecommunications, Institut National de la Recherche Scientifique, 1650 Boulevard Lionel-Boulet, Varennes, Quebec, J3X 1S2, Canada

^c School of Chemistry and Material Science, Guizhou Normal University, Guiyang, 550001, P.R. China

^d Department of Electrical Engineering, École de Technologie Supérieure, 1100 Notre-Dame Ouest, Montreal, Quebec, H3C 1K3, Canada

^e College of Physics and the State Key Laboratory, Qingdao University, No. 308 Ningxia Road, Qingdao, 266071, P.R. China

ARTICLE INFO

Keywords:

Graphene oxide
Cobalt
Earth-abundant electrodes
Charge transfer
Photoelectrochemical cells

ABSTRACT

Low-cost nanostructured hybrid materials and the optimization of their structural design present an opportunity to achieve high performance and stable renewable energy devices. Here we used electrospinning to homogeneously embed graphene oxide (GO) nanosheets within the one-dimensional structure of cobalt-based nanohybrids (CoNHs). In particular, we focus on the performance of these nanohybrids in Na₂S/Na₂SO₃ aqueous electrolyte (pH = 13) due to its wide application in photocatalytic and photoelectrochemical (PEC) devices. We demonstrate that the addition of GO can remarkably reduce the charge transfer resistance from 4.4 Ω to 2.5 Ω for the 0 wt% GO/CoNHs and the 12 wt% GO/CoNHs, respectively. Furthermore, the CoNHs display outstanding electrochemical long-term stability, as the overpotential required to keep $J = -10 \text{ mA cm}^{-2}$ is invariable for over 42 h. The structural characterization of the nanohybrids indicates that during continuous operation, the CoNHs rebuild and regenerate *in situ* leading to the formation of two-dimensional nanostructures comprising a mixture of cobalt chalcogenides (Co₃S₄ and CoS₂). The integration of the CoNHs in a quantum-dot based PEC cell and an alkaline electrolyzer (1 M KOH) demonstrates the versatility and viability of these alternative electrodes toward active and solar-driven fuel generation.

1. Introduction

Due to their outstanding catalytic, optical and electronic properties, nanohybrids based on transition metal oxides (TMOs) and transition metal chalcogenides (TMCs) are attractive materials for the development of earth-abundant electrodes in a variety of renewable energy technologies [1–3]. Understanding structure/property relationships within the different components and with their interfaces, can lead to great improvements in the performance and long-term stability of the devices in their operational environment [2–8]. Among various TMOs and TMCs, cobalt oxides and cobalt chalcogenides are favorable materials for use in a wide variety of electrochemical and photoelectrochemical (PEC) systems [8–18]. Both cobalt-based compounds have been shown to be promising electrocatalysts for the hydrogen evolution reaction (HER) [11–16]. Additionally, cobalt chalcogenides have been

shown to exhibit high electrocatalytic activity and stability toward the sulfide/polysulfide electrolyte commonly used in quantum dot sensitized solar cells (QDSCs) [9,19]. Coupling of these cobalt-based compounds with carbon nanomaterials favors fast transport of charge carriers, thanks to the high electrical conductivity, large surface area, structural flexibility and strong tolerance to acid/alkaline environments which are properties highly desirable to derive advanced hybrid electrocatalysts [20–24]. Similarly, carbon substrates not only act as a conductive support but also interact with TMO or TMC nanoparticles through strong coupling effects between both components [24–26]. Such interactions induce more-favorable electrocatalytically active sites [20,22].

Recently, there has been tremendous progress in the photocatalytic and PEC generation of hydrogen (H₂) using semiconductor chalcogenides, in the form of quantum dots (QDs) [27–35]. Unfortunately, a

* Corresponding authors at: Institute of Fundamental and Frontier Sciences, University of Electronic Science and Technology of China, Chengdu, 610054, P.R. China.

** Corresponding author.

E-mail addresses: hgzha@qdu.edu.cn (H. Zhao), zwmwang@uestc.edu.cn (Z.M. Wang), rosei@emt.inrs.ca (F. Rosei).

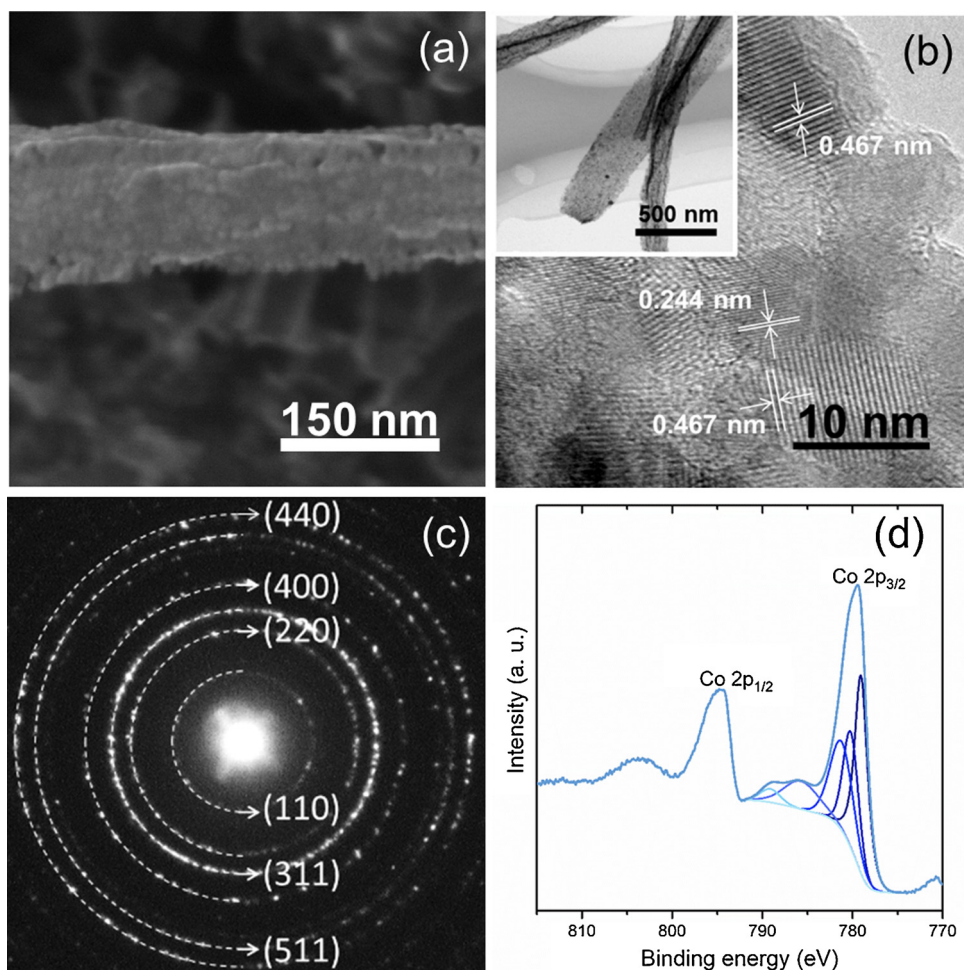


Fig. 1. Structural characterization of 0 wt% GO/CoNHs. (a) SEM image of an individual cobalt-based nanohybrid. (b) High resolution TEM image showing the lattice fringe separation of Co_3O_4 . (c) Corresponding SAED patterns. (d) High resolution XPS spectrum.

major limitation in this type of system is that the reduction of pure water to produce H_2 is usually rather inefficient [36]. Using sacrificial molecules, e.g. $\text{Na}_2\text{S}/\text{Na}_2\text{SO}_3$, in aqueous solution can remarkably improve the rate of H_2 production, as holes are scavenged by these molecules and charge carrier recombination can be greatly reduced. Although significant progress has been made in this area regarding the enhanced performance of photoactive semiconductor chalcogenides, until now there have been few studies of electrocatalysts that possess long-term stability, specifically in PEC cells [37–40]. Most QD-based PEC devices for H_2 generation have been studied with a platinum counter-electrode, therefore in the future, the widespread application of this system will be compromised by the scarcity and high cost of this electrocatalyst [4,6,27,34]. Additionally, the sulfur species present in the electrolyte are known to chemisorb on platinum, consequently reducing its electrocatalytic activity [39,41]. Copper sulfide electrodes (Cu_xS_x) have the potential of replacing platinum in PEC cells [17,38–41]. However, these electrodes can poison the photoactive surface through both diffusion- and field-assisted deposition of Cu_xS_x , resulting in gradual deterioration of the system's performance [5,38]. Additionally, Cu_xS_x electrodes (often found as sulfurized Cu or brass foils) suffer from mechanical instability [9,38]. The development of economic and operationally competitive earth-abundant electrodes depends on factors, such as cost, ease of synthesis, and more importantly, electrocatalytic activity and stability [4,42]. By tailoring both the chemical composition and structure of an electrocatalyst, it is possible to achieve an unprecedented catalytic reactivity and simultaneously attain the largest number of exposed active sites in a certain

geometric electrode area [2,25].

Spinel Co_3O_4 comprises two types of cobalt ions with different oxidation states, namely: Co^{2+} and Co^{3+} [10]. Therefore, it is expected to share a similar catalytic mechanism previously proposed [43], involving cobalt complex catalysts with the same oxidation states in identical alkaline media ($\text{Na}_2\text{S}/\text{Na}_2\text{SO}_3$). In general, during cathodic polarization, the electrons can be easily transferred to Co_3O_4 , leading to the formation of a hydride at the Co center, consequently favoring H_2 generation [43,44]. Herein, we propose a convenient approach that consists in electrospinning a cobalt precursor and graphene oxide (GO) directly onto large-area carbon fiber paper (CFP) substrates. This nanostructuring approach allows to homogeneously disperse GO nanosheets and embed them within Co_3O_4 nanoribbons, consequently extending the electrocatalytically active sites due to the high aspect ratio of the nanoribbons. In addition, this morphology enhances charge transfer and maintains the mechanical robustness of the electrode arising from the intrinsic properties of the GO nanosheets. Accordingly, we optimized the GO concentration to enhance charge transfer within the Co_3O_4 nanoribbons. We subsequently demonstrate the effective generation of H_2 under long-term operation using these cobalt-based nanohybrids (CoNHs) under alkaline conditions (0.25 M Na_2S / 0.35 M Na_2SO_3 , pH = 13) that are typically used for semiconductor chalcogenide photoactive components. We further explain that in this sulfur containing medium the CoNHs can undergo an *in situ* conversion from Co_3O_4 into cobalt chalcogenides and the nanoribbon structure can transform into nanosheets, thereby maintaining large active surfaces. As a proof of concept we implemented these electrodes in a QD-based

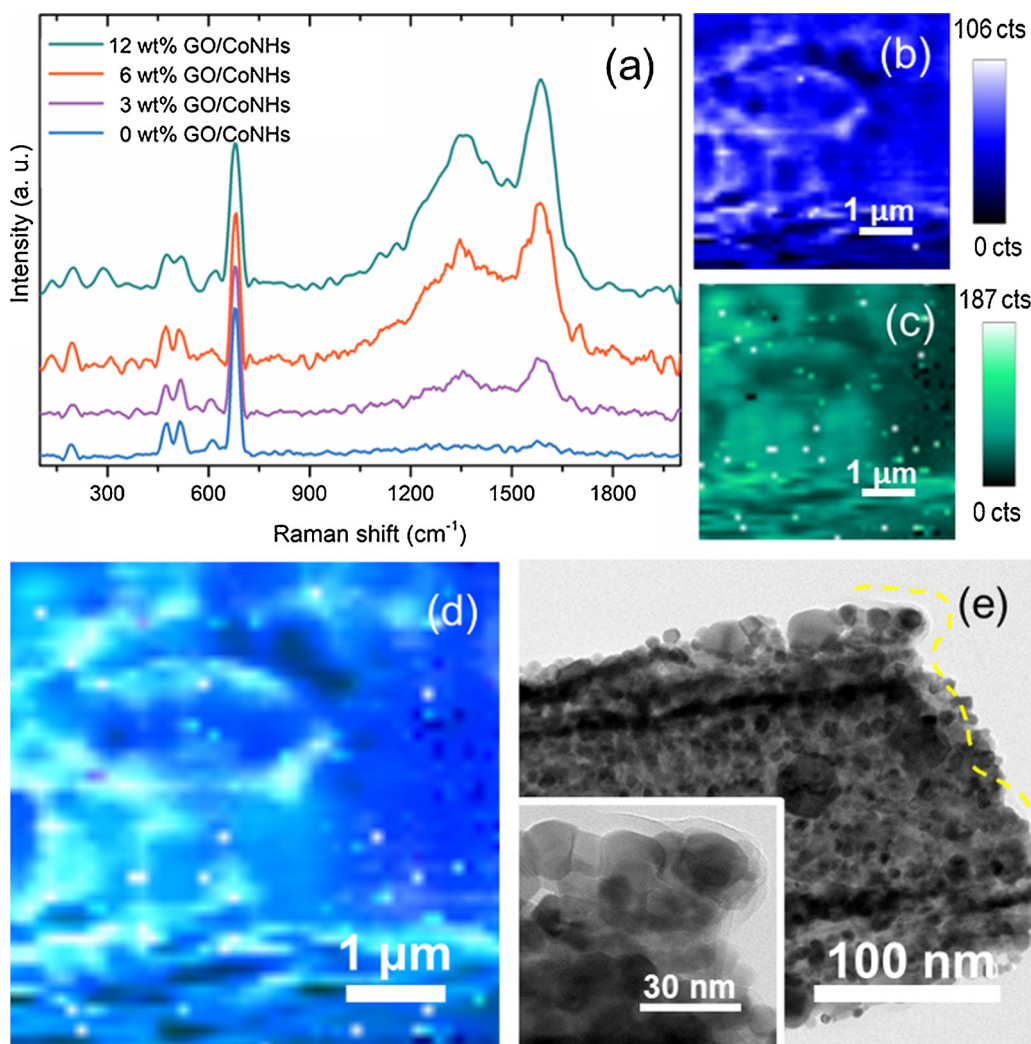


Fig. 2. Structural characterization of the different CoNHs. (a) 1D Raman mapping of CoNHs obtained with different GO concentrations. 2D Raman mapping of 12 wt % GO/CoNHs filtered according to: (b) Co_3O_4 : F_{2g} (680 cm^{-1}) band, (c) GO: G (1585 cm^{-1}) band and (d) composite image. (e) TEM images of 12 wt% GO/CONHs, inset corresponding to the highlighted yellow area (protruding GO nanosheets). (For interpretation of the references to colour in this figure legend, the reader is referred to the web version of this article.)

PEC cell for H_2 generation. Furthermore, we expanded the application of the large-area GO/Co-based electrodes in a solar-driven electrolyzer for water splitting in 1 M KOH to demonstrate the versatility of these nanohybrids.

2. Experimental section

2.1. Materials

Cobalt (II) nitrate hexahydrate ($\text{Co}(\text{NO}_3)_2 \cdot 6\text{H}_2\text{O}$, 98%), polyvinylpyrrolidone (PVP, $M_w \sim 1\ 300\ 000$), graphite powder (99.99%), potassium permanganate (K_2MnO_4 , 99.0%), hydrogen peroxide (H_2O_2 , 30%), sulfur (100%), oleylamine (70%), cadmium oxide (99%), oleic acid ($\geq 99\%$), rhodamine 6 G (99%), octadecene ($\geq 95\%$), selenium pellets ($\geq 99.999\%$), trioctylphosphine oxide (99%), trioctylphosphine (97%), zinc nitrate hexahydrate ($\text{Zn}(\text{NO}_3)_2 \cdot 6\text{H}_2\text{O}$, 98%), sodium sulfide nonahydrate ($\text{Na}_2\text{S} \cdot 9\text{H}_2\text{O} \geq 98\%$), sodium sulfite (Na_2SO_3 , $\geq 98\%$), hexane, toluene, methanol, acetone, ethanol and isopropanol, were obtained from Sigma Aldrich Inc. Ti-Nanoxide BL/SC was bought from Solaronix. TiO_2 paste (18NR-AP) was supplied by Dyesol. Fluorine doped tin oxide (FTO) coated glass substrates with sheet resistance $10 \Omega \text{sq}^{-1}$ were bought from Pilkington glasses. CFP substrates (Spectracarb 2050A-0550) were obtained from Fuel Cell Store. All

chemicals were used as purchased.

2.2. Carbon/Co-based electrode preparation

GO was obtained by first synthesizing graphite oxide by using the modified Hummers method [45]. A graphite oxide dispersion of 10 mg/mL was sonicated for 30 min, followed by centrifugation for 2 h (7000 rpm). Water was removed to obtain a dispersion of 65 mg mL⁻¹ which is further subjected to sonication for 2 h. The resulting GO aqueous dispersion (5 mL, 65 mg mL⁻¹) was further dispersed in ethanol (7 mL). Subsequently we obtained solutions with different concentration of GO ($\sim 3 \text{ wt\%}$, $\sim 6 \text{ wt\%}$ and $\sim 12 \text{ wt\%}$) compared to the amount of cobalt precursor ($\text{Co}(\text{NO}_3)_2 \cdot 6\text{H}_2\text{O}$) to produce GO/CoNHs. The content of each chemical is included in Supplementary materials Table S1. For example, to obtain 12 wt% GO/CoNHs, the GO ethanolic/aqueous dispersion (0.8 mL, 27.87 mg mL⁻¹) was re-dispersed in ethanol (2.293 mL) under sonication for 1 h. Subsequently, PVP (201 mg) was added and the dispersion was kept under stirring (300 rpm) for 1 h. Then $\text{Co}(\text{NO}_3)_2 \cdot 6\text{H}_2\text{O}$ (164.5 mg) was added and the resulting precursor solution was kept under stirring for 20 h. CFP substrates were cut into pieces of $20 \times 15 \text{ mm}^2$, then they were ultrasonically cleaned in acetone for 15 min, rinsed in distilled water and dried at 120 °C for 10 min. Finally, they were treated in an Ossila UV Ozone cleaning

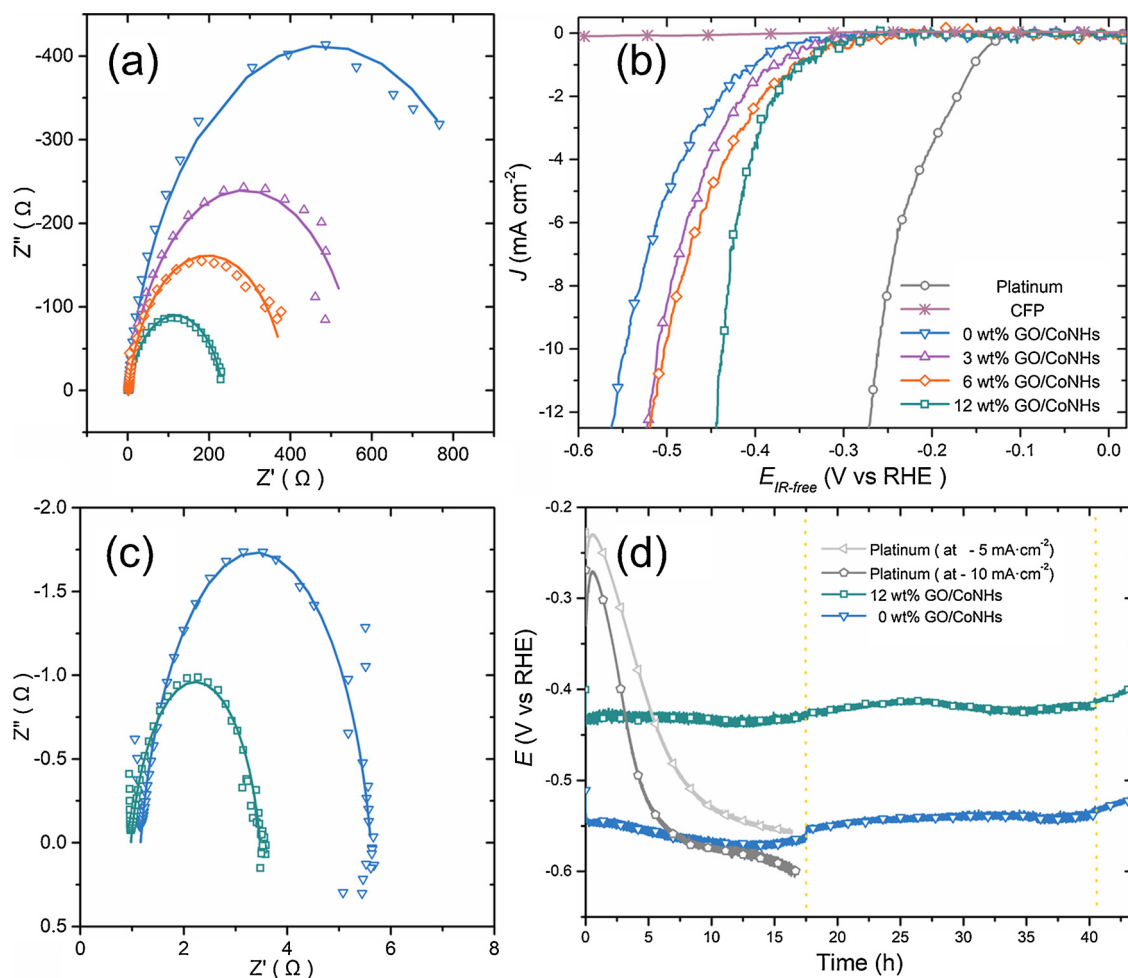


Fig. 3. Electrochemical characterization of the CoNHs in 0.25 M Na₂S / 0.35 M Na₂SO₃ (pH = 13). (a) Nyquist plots of the different CoNHs obtained from EIS at the OCP (694 mV vs RHE) showing the measured (unfilled symbols) and the corresponding fitted data (solid lines). (b) Polarization curves of the different nanohybrid electrodes compared to the platinum electrode (c) Nyquist plots obtained from EIS at the HER potential (-450 mV vs RHE) (d) Long-term stability measurements of the CoNHs to maintain $J = -10 \text{ mA cm}^{-2}$ and performance degradation of the platinum electrode at different J ; dotted yellow lines indicate the time at which electrolyte was added to recover the initial volume. (For interpretation of the references to colour in this figure legend, the reader is referred to the web version of this article.)

system, for 20 min prior to electrospinning. The as-prepared GO/Co/PVP precursor solution was electrospun using a Spraybase, Profector Life Sciences electrospinning unit with a 26 G needle, at a flow rate of 0.1 mL h⁻¹ and an applied voltage of 20 kV over a collection distance of 15 cm, during 30 min. The CoNHs were collected on the CFP and then they were heated up to 500 °C for 30 min under air atmosphere, to remove the polymer and to produce the nanoribbons.

2.3. Structural characterization

The morphology of CoNHs was characterized by field emission scanning electron microscopy (FESEM) using a JEOL JSM7401 F FE-SEM equipped with an energy-dispersive X-ray spectrometer (EDS). Transmission electron microscopy (TEM) and selected area electron diffraction (SAED) were performed using a JEOL JEM-2010 TEM. Raman spectra and images were obtained in a WITec Alpha 300 micro-Raman system equipped with a 532 nm fiber-coupled laser for excitation. X-ray diffraction (XRD) patterns were acquired using a Bruker D8 Advance X-ray diffractometer equipped with Cu K_α radiation. X-ray photoelectron spectroscopy (XPS) was performed in a VG Escalab 220i-XL equipped with a hemispherical analyzer recorded for a twin anode X-ray source. All the spectra were corrected to assign the adventitious C 1 s spectral component (C-C,C-H) a binding energy of 284.8 eV [46].

The fine structure of the photoelectron lines was analyzed using Casa XPS software (2.3.18 Version).

2.4. Electrochemical characterization

The electrochemical tests were conducted in a three-electrode cell using the different CoNHs deposited onto CFP or a platinum plate as the working electrode, a saturated Ag/AgCl reference electrode and a platinum plate as the counter-electrode. The measurements were performed using a Solartron SI 1287 Potentiostat/Galvanostat. Prior to any measurement, the platinum counter-electrode was cleaned in 0.5 M H₂SO₄ by using three cyclic voltammetry steps from 764 mV to 1964 mV vs RHE at three scan rates: 200 mV s⁻¹ × 50 cycles, 100 mV s⁻¹ × 5 cycles and 50 mV s⁻¹ × 5 cycles. Each measurement was performed in 0.25 M Na₂S / 0.35 M Na₂SO₃ (49 mL, pH = 13) electrolyte which was purged with N₂ for 30 min prior any measurement and continuously during the tests. Firstly, electrochemical impedance spectroscopy (EIS) of as-prepared CoNHs was performed in potentiostatic mode at the open circuit potential (OCP) of each sample (unless stated), applying a sinusoidal voltage with an amplitude of 10 mV and a scanning frequency from 100 kHz to 100 mHz. The spectra were modeled using a simplified Randles equivalent circuit, which consists of a resistor (R_s) in series with a parallel arrangement of a

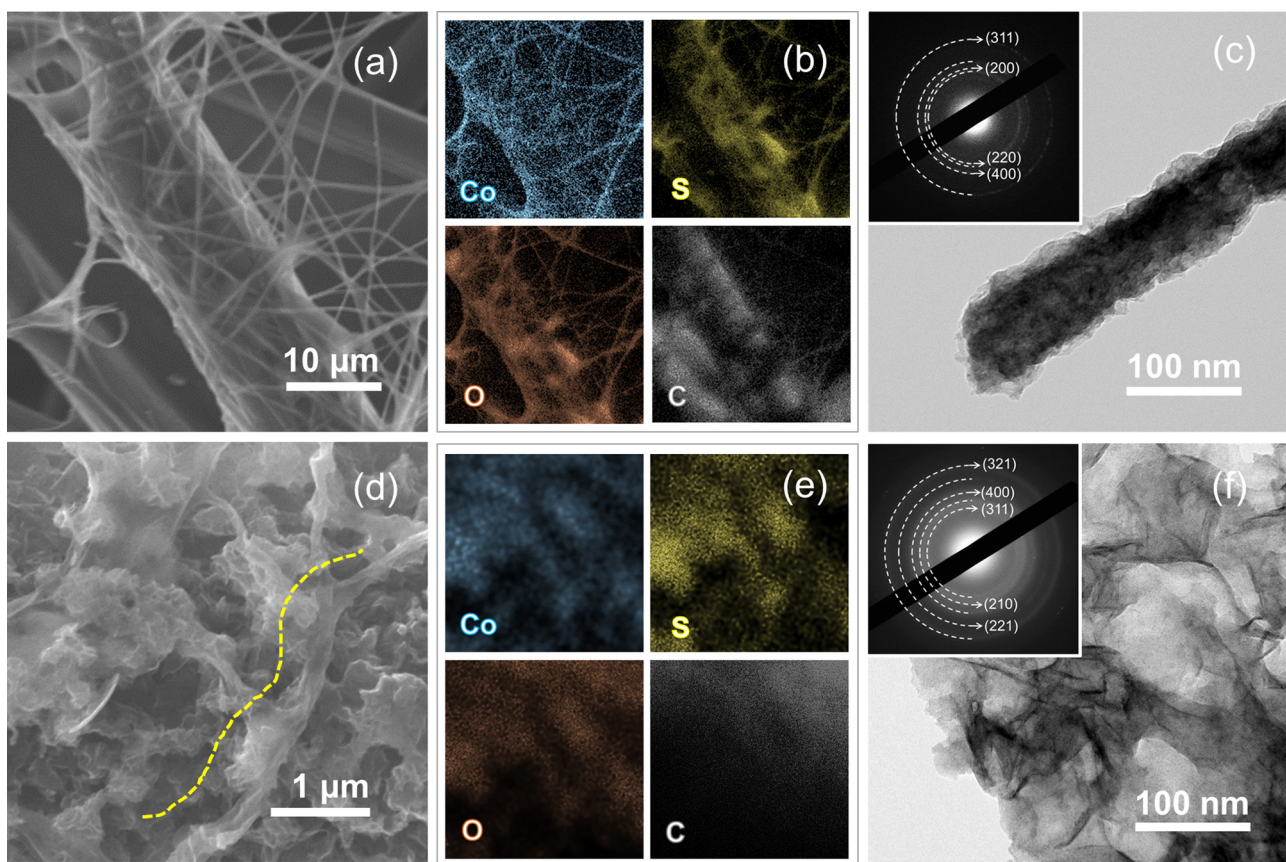


Fig. 4. Morphology and crystalline phase changes of the 12 wt% GO/CoNHs after electrochemical tests. (a) SEM (b) EDS and (c) TEM images after short-term stability tests (4 h, after polarization curves). (d) SEM (e) EDS and (f) TEM images after long-term stability test (40 h, after chronopotentiometry). Insets in TEM images show their respective SAED patterns.

resistor (R_{ct}) and a constant phase element (CPE) and it was fitted using the Zview software. Subsequently, the different CoNH samples were first subjected to a series of cyclic voltammograms at a scan rate of $20 \text{ mV s}^{-1} \times 5$ cycles and broadening the applied potential window from their OCP towards the HER potential, increasing in steps of 100 mV. Lastly, the polarization curves reported in this work were obtained after the third linear scan sweep from 14 mV to -606 mV vs RHE at a scan rate of 0.1667 mV s^{-1} . The analyzed curves were corrected to the ohmic drop and background current, as indicated in the Supplementary materials (Fig. S1). Solar-driven measurements were performed under simulated sunlight (1 sun = 100 mW cm^{-2} , AM 1.5 G) using a Scientech SLB-300 A compact solar simulator class AAA. A Scientech Si reference diode was used to verify the standard 1 sun illumination before each measurement. Two-electrode cell measurements were conducted in 1 M KOH using CoNHs on CFP as both cathode and anode.

3. Results and discussion

The development of high-performance and stable nanohybrids which are directly deposited onto conducting substrates is favorable to reduce fabrication costs of energy conversion devices [3,42]. Electrospinning was used to produce large aspect ratio nanostructures from a precursor aqueous/ethanolic solution containing GO, $\text{Co}(\text{NO}_3)_2$, and PVP. The one-dimensional (1D) nanohybrids were electrospun onto large-area CFP and were heated up to 500°C and kept at this temperature for 30 min in air to remove the polymer and produce semiconductor nanoribbons with width ranging from 150 to 250 nm, as seen in Fig. 1a. TEM images in Fig. 1b indicate that the nanoribbons are composed of nanoparticles with average size of $\sim 10 \text{ nm}$. The high-

resolution TEM (HRTEM) image reveals clear lattice fringes with distances of 0.466 and 0.267 nm, which match well with the (111) and (311) planes of Co_3O_4 (JCPDS 042-1467), respectively. The corresponding SAED patterns are included in Fig. 1c. High-resolution Co 2p spectrum (Fig. 1d) show spin-orbit splitting into $2p_{1/2}$ and $2p_{3/2}$ components, which qualitatively contain identical chemical information [47]. Consequently, only the higher-intensity Co $2p_{3/2}$ peak was curve-fitted, including its shake-up satellites. The Co $2p_{3/2}$ peak was resolved in a first contribution at 779.6 eV, attributed to Co^{3+} state, and in two additional peaks located at 780.9 and 782.2 eV, ascribed to Co^{2+} state [48]. In the higher binding energy region, two peaks are required to fit the satellites. These additional spectral lines have been ascribed either to a coupling between unpaired electrons in the atom (multiplet splitting) or a multiple electron excitation (the so-called ‘shake-up’) [46,47]. A broad satellite peak at 785.5 eV and a lower satellite at around 789.9 eV was found in the samples. From the XPS, SAED and XRD results (Supplementary materials, Fig. S2) we can confirm the presence of the Co_3O_4 spinel phase.

The incorporation of carbon nanomaterials has been proven to be effective to overcome the poor electronic conductivity of semiconductors [26,49–53]. Specifically, hybrids of semiconductors with GO have demonstrated enhanced electrocatalytic performance [24,54]. Accordingly, we fabricated CoNHs with different content of GO. As seen in Fig. 2a, Raman spectra exhibit five peaks at 195, 478, 519, 619 and 680 cm^{-1} corresponding to the F_{2g} , E_g , F_{2g} , F_{2g} , and A_1 active modes of Co_3O_4 , respectively [55]. Additionally, the characteristic peaks of GO are observed at 1356 and 1585 cm^{-1} . These are associated to the D band arising from the sp^3 hybridized carbon atoms in the case of the former and the G band related to the sp^2 domains in the case of the latter [23,56]. Two-dimensional (2D) Raman mapping revealed that the

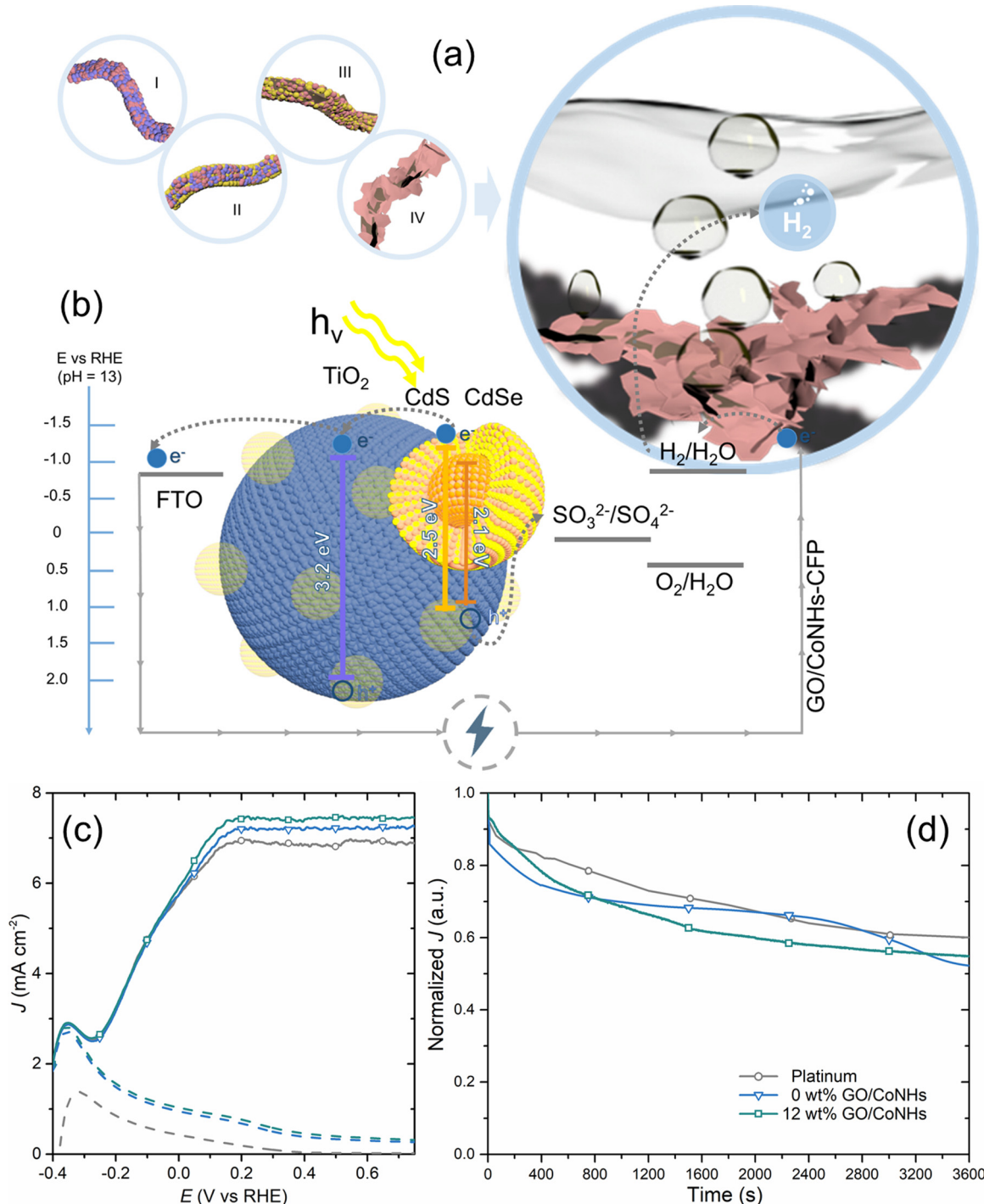


Fig. 5. (a) Structural evolution of CoNHs in 0.25 M Na₂S / 0.35 M Na₂SO₃. QD-based PEC generation of H₂: (I) as-prepared GO/CoNHs, (II) electrochemical activation, (III) growth of cobalt sulfides and (IV) *in situ* regeneration into nanosheets. (b) Band alignment of the QD-based PEC system, using the bulk energy levels; arrows indicate the electron and hole transfer processes. Inset showing H₂ evolution at the GO/CoNHs. (c) Current density (*J*) vs applied potential (*E*) in a PEC system based on a CdSe/CdS-TiO₂ photoanode, employing different CEs. (d) Stability measurements: *J* as a function of time at 200 mV vs RHE under 100 mW cm⁻², AM 1.5 G.

location of the Co₃O₄ nanoribbons (Fig. 2b) coincide with the location of the GO nanosheets (Fig. 2c), indicating that GO was homogeneously dispersed within the nanoribbons. This is confirmed by the composite image displayed in Fig. 2d. TEM images included in Fig. 2e and Supplementary materials Figs. S3 and S4 further corroborated that most GO sheets were embedded within the Co₃O₄ and might have folded within the nanoribbon structure at the moment of electrospinning. This type of large-area readily integrated electrodes are advantageous to avoid the

time- and cost-consuming synthesis processes, such as hydrothermal synthesis [1,14,19] and pyrolysis [13,21,22] which are among the typically used methods to synthesize TMOs and TMCs. Compared to the electrodes relying on powder electrocatalysts and polymer binders, these binder-free electrodes diminish the series resistance, while also allowing for a higher use of the active sites during the H₂ evolution process [3]. Additionally, this type of nanohybrids directly deposited onto conductive substrates provide a platform for further modification

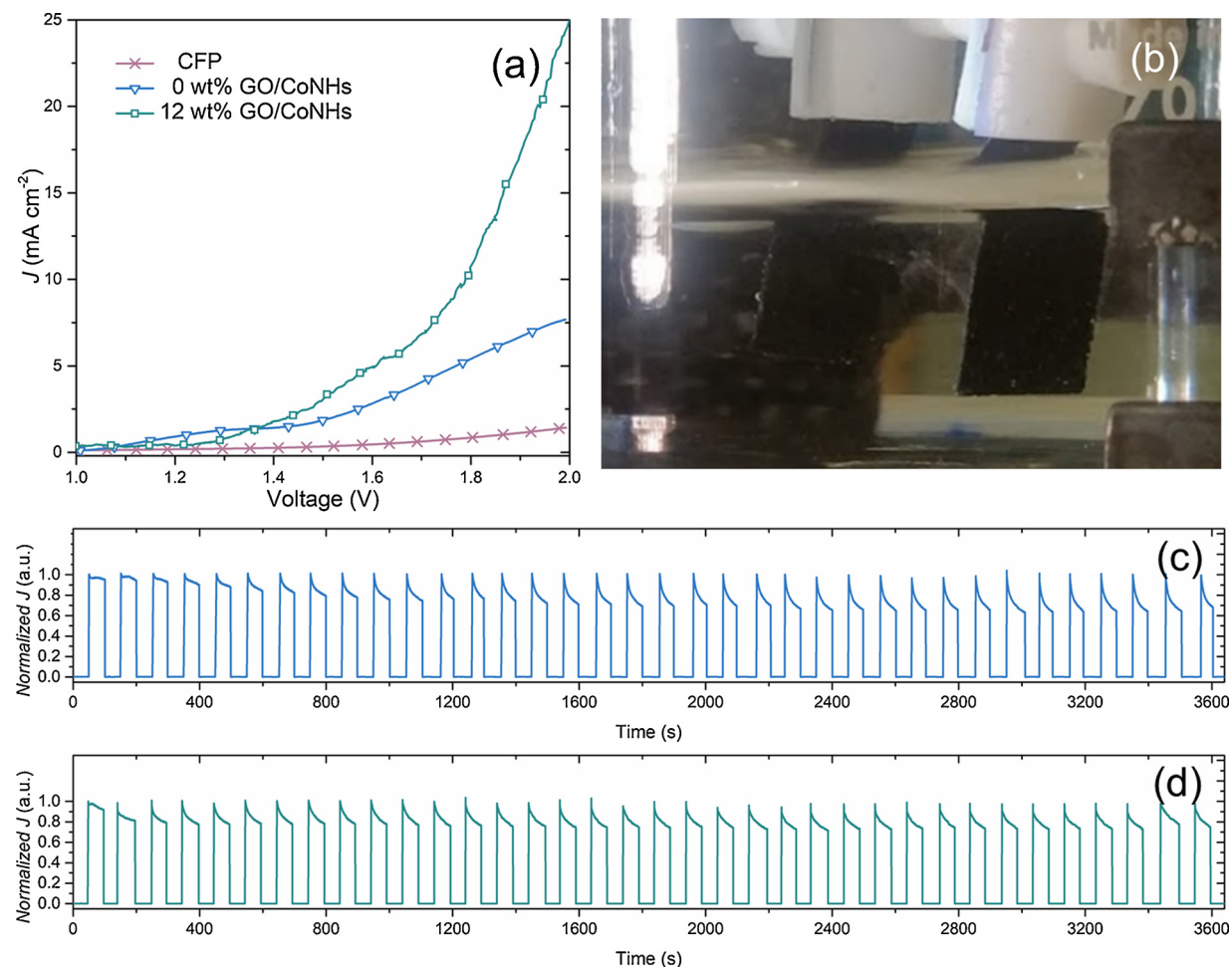


Fig. 6. (a) Overall water splitting in a two-electrode cell using the as-prepared CoNHs as both anode and cathode in 1 M KOH. (b) Digital photograph of the PV-biased two-electrode cell showing the bubbles of H_2 and O_2 evolved gasses. Stability performance of a PV-biased water splitting under simulated light (100 mW cm^{-2} , AM 1.5 G) of the (c) 0 wt% GO/CoNHs and (d) 12 wt% GO/CoNHs.

by using other practical methods such as electrodeposition to tune the electrocatalyst loading and the micro/nanostructure of the electrode (Supplementary materials, Fig. S5).

Several recent studies have shown the efficiency of hybridizing cobalt with carbon nanomaterials towards the HER (Supplementary materials Table S2) [12–14]. Most of these systems work with KOH or H_2SO_4 aqueous solutions. However neither of these electrolytes are often used for long-term stable photocatalytic and/or PEC applications which usually involve photoactive species based on TMCs. The stability of these systems depends on using aqueous electrolytes with sulfur containing compounds such as $\text{Na}_2\text{S}/\text{Na}_2\text{SO}_3$. To effectively evaluate the electrochemical performance of the different electrodes, we examined their behavior toward HER in this type of alkaline media. First, the effect of the incorporation of GO within the CoNHs was investigated by performing EIS measurements of the as-prepared electrodes, as included in Fig. 3a. The semicircle in the Nyquist plot, attributed to the charge transfer resistance R_{ct} , is related to the kinetics of the electron transfer and a lower diameter semicircle corresponds to a faster reaction rate [12]. The R_{ct} value of the CoNHs is significantly reduced by the addition of GO (Supplementary materials Table S3). This trend is consistent with the reduced overpotential for HER with the addition of GO, as reported in the polarization curves included in Fig. 3b. The overpotential needed to maintain a $J = -10 \text{ mA cm}^{-2}$ decreased $\sim 100 \text{ mV}$ for the highest content of GO (12 wt%) used compared to 0 wt% GO/CoNHs. As also suggested in Supplementary materials Table S2, better performance might be attained at the expense of higher electrocatalyst content, compared to our proposed hybrid electrode (electrocatalyst

mass at least 10 times lower, see Supplementary materials Note 1). The linear regions of the Tafel plots of the different CoNHs are displayed in Supplementary materials Fig. S6. These plots were fitted into the Tafel equation ($\eta = a + b \ln J$, where J is the current density and b is the Tafel slope). The Tafel slope decreases gradually from 74 mV/dec in the 0 wt% GO/CoNHs to 59 mV/dec in the 12 wt% GO/CoNHs.

Furthermore, we carried out EIS analysis when applying the potential for HER, the R_{ct} decreases from 4.4Ω in the 0 wt% GO/CoNHs to 2.5Ω in the 12 wt% GO/CoNHs. The enhanced performance of the GO/CoNH electrode was achieved by using $\leq 12 \text{ wt\%}$ GO compared to the cobalt precursor, whereas most of the investigations reported until now focused on composites where the carbon acts as a support or provides encapsulation of the electrocatalyst [13,21,22]. While the incorporation of GO has been shown to be effective to overcome the poor electron-conductive properties in electrodes for hydrogen generation [54], we cannot exclude other mechanisms that may favour such dramatic enhancement in the charge transfer properties of our electrodes. Among other possibilities that contribute to this effect could be the *in situ* reduction of GO or the formation of metallic CoS_2 during the HER which can successfully enhance the electrical conductivity of GO, similarly to the previously found synergistic behavior produced by an ensemble of metallic nanoparticles distributed on the graphene surface [57]. Online gas chromatography was used to measure H_2 evolution when applying a constant potential and the associated Faradaic efficiencies (η_{Faradaic}) were determined by comparing the amount of gas produced experimentally with the theoretically calculated values (see the experimental section in the Supplementary materials for details). Only H_2 gas was

detected, and as displayed in Supplementary materials Fig. S7, after half an hour the H₂ evolution stabilizes and reaches a $\eta_{\text{Faradaic}} = \sim 90\%$, corroborating the remarkable performance of the GO/CoNHs as alternative electrocatalysts for H₂ generation.

Generally, the enhanced charge transport observed as the GO content increases can be attributed to both the synergistic effect between the carbon nanostructure and the electrocatalyst, as well as the overall architecture of the electrode. Specifically, the oxygen-containing functional groups arising from the sp³ domains within the matrix of graphene allow for a homogeneous dispersion of the nanosheets within the network of CoNHs. Subsequently, the conducting π -states from sp² carbon sites within GO sheets mediate the enhanced charge transport and the catalytic activity of Co²⁺ within CoNHs, allowing efficient H₂ evolution, which is further favored by the high aspect ratio of the nanohybrids [58]. Additionally, using CFP as the substrate permits efficient electron pathways due to the conductive network of carbon fibers while keeping effective electrolyte access to the active CoNH electrocatalyst; the latter characteristic has been demonstrated to account for improved operational stability by promoting the easy release of evolved H₂ bubbles [12]. This is illustrated in Supplementary materials Fig. S8, where we show the surface covered in microbubbles in the GO/CoNHs supported in CFP, compared to the larger size bubbles in the platinum plate that commonly pin to planar electrodes diminishing their active surface area. Another advantage of our readily integrated CoNH electrocatalysts within the CFP substrate is the elimination of the use of a rotating disk electrode and/or planar substrates for the HER.

We also studied the electrochemical performance of both 0 wt% GO/CoNHs and 12 wt% GO/CoNHs when they were directly deposited on FTO substrates, as shown in Supplementary materials Fig. S9. The trend remains similar to that achieved in the electrodes using CFP, however these electrodes exhibit poor performance, possibly related to the detachment of the electrocatalyst from the substrate. Stable operation over extended periods of time is also a critical factor to consider when designing electrodes. Consequently we conducted chronopotentiometry measurements consisting of applying a constant cathodic current density and verifying that the resulting overpotential is maintained similar to the value obtained in the polarization curves of the different electrodes. Fig. 3d shows that the performance of platinum decays within the first 35 min of the experiment, when maintaining a $J = -10 \text{ mA cm}^{-2}$; over prolonged operation this electrode requires even a higher overpotential than that needed for H₂ generation in 0 wt % GO/CoNHs after 17 h. Similar behavior was observed even when we lowered the current density ($J = -5 \text{ mA cm}^{-2}$). The electrocatalytic activity of the platinum electrode is reduced by the chemisorbed sulfur species that strongly adsorb to its surface (see Supplementary materials Fig. S10). In contrast, both 0 wt% GO/CoNHs and 12 wt% GO/CoNHs showed remarkable performance for over 42 h. A slight variation in the applied overpotential is related to the consumption of the electrolyte.

Subsequently, we studied the morphological, structural and charge transfer characteristics of the electrodes after electrochemical stability tests. As observed in Fig. 4a and b, after the short-term stability tests ($\sim 4 \text{ h}$), the nanoribbons remain attached to the CFP substrate, the morphology does not show any variation according to SEM images, whereas TEM images (Fig. 4c) reveal a rougher morphology in the nanoribbons compared to those before any test. The SAED patterns of the 12 wt% GO/CoNHs consist of rings with d-spacings of 0.167 and 0.277 nm corresponding to (311) and (200) lattice spacing of CoS₂ (JCPD 041-1471), 0.236 nm consistent with the (400) lattice spacing of Co₃S₄ (JCPDS-047-1238) and 0.285 nm matching the (220) lattice spacing of Co₃O₄ (JCPDS- 042-1467). After long-term stability tests ($\sim 42 \text{ h}$), as seen in the SEM and EDS images the morphology of the electrocatalyst changes into 2D nanosheets with a rough and curved surface, corroborated with TEM images, which show a clearer image of the nanosheet structure with ultrathin thickness, as per Fig. 4d-f. Additionally, after the 42 h stability test, SAED patterns displayed rings with d-spacings of 0.148, 0.184, 0.250 nm corresponding to (321),

(221) and (210) lattice spacing of CoS₂, 0.202 nm consistent to (400) lattice spacing of Co₃S₄ and 0.284 nm corresponding to (311) lattice spacing of Co₃O₄. A similar formation of a mixture of cobalt sulfides was found in the 0 wt% GO/CoNHs (Supplementary materials Fig. S11). EDS measurements, displayed in Supplementary materials Fig. S12, also corroborated the increased presence of sulfur as the electrochemical tests were longer. We also carried out chemical stability tests, during which the nanohybrid electrodes were kept in the electrolyte for 2 days, and we found out that the structural composition remained the same as the as-prepared Co₃O₄ nanoribbons, confirmed by the TEM images and SAED patterns (Supplementary materials Fig. S13). Additionally, as seen in Supplementary materials Fig. S14, we identified that there was a decrease of the R_{ct} possibly related to the formation of the cobalt sulfides which possess higher conductivity than cobalt oxide [3,11].

In agreement with our structural characterization, at pH = 13 and at the potentials studied in this work, Pourbaix analysis suggests that the Co₃O₄ goes into transformation to Co(OH)₂ [59]. Subsequently, the presence of Na₂S/Na₂SO₃ electrolyte leads to the partial formation of a combination of cobalt sulfides. In the absence of an applied bias, Co₃O₄ is stable and the crystalline phase remains unchanged. Earlier studies proposed that, due to their versatile oxidation states, Co-based compounds possess the ability to self-assemble and regenerate (or “self-repair”) *in situ*, such that the catalytic reactions can proceed at a steady rate [59,60]. From the structural characterization we can draw the conclusion that upon the cathodic conditions, in Na₂S/Na₂SO₃ in aqueous solution, Co ions rebuild and allow the growth of cobalt sulfide nanosheets. Such change does not compromise the performance of the electrode and endows it with long-stable operation for H₂ production (Fig. 5a). Additionally, our as-prepared Co₃O₄ structured electrodes represent an advantage to the readily CoS₂ electrodes which are air and moisture sensitive and easily convert to CoSO₄ which is inactive for HER [61].

Consequently, as a proof of concept we verified the performance of our CoNHs in a QD-based PEC device for H₂ generation. A standard QD-based PEC device with platinum as counter-electrode was used as benchmark, or control. Fig. 5b shows the working principle of this device, where the photogenerated electrons in CdSe/CdS QDs adsorbed into a TiO₂ mesoporous film, move toward the external circuit to re-enter the system at the counter-electrode where water is reduced to produce H₂. The PEC activity is typically studied in a three-electrode cell under simulated illumination, where the QD/TiO₂ photoanode acts as the working electrode in which a potential is scanned and measured with respect to a reference electrode, and in this case, our different CoNHs deposited on CFP were used as counter-electrode, as included in Fig. 5c. The resulting photocurrent density (J) is related to the amount of H₂ evolved at the counter-electrode. In this cell configuration the PEC behavior using different CoNHs is not compromised, at 200 mV vs RHE, J reaches its saturation $\sim 7.5 \text{ mA cm}^{-2}$. A similar behavior is also obtained during long-term stability tests, displayed in Fig. 5d, where the decay in the performance is mainly related to the QD/TiO₂ photoanode [27–32]. This stability test allow us to corroborate the solidity of the PEC device, without any contamination from the counter-electrode in the photoanode, as previously reported [9,38].

We also examined the viability of the electrodes towards water splitting in alkaline media (1 M KOH) by using a two-electrode configuration where the CoNH electrodes worked as both anode and cathode (Fig. 6a). A current density of $J = 10 \text{ mA cm}^{-2}$ was achieved by applying an external bias of 1.79 V. Although this voltage is higher than other state of the art electrolyzers (due to higher catalyst loading), the value is within the range of commercial electrolyzers, *i.e.* 1.7–1.9 V [62], in this case using a much lower amount of electrocatalyst (see Supplementary materials Table S4).

Finally, we adapted a silicon photovoltaic (PV) module connected to the CoNHs electrodes to drive the photoelectrochemical reaction (Fig. 6b and Supplementary materials Fig. S15a). Fig. 6c shows that within an hour the performance is stabilized and maintains 94% of the

initial potential. The predicted operating current density of the combined system (normalized to the total illuminated area of the solar cells) is defined by the intersection of the *J-V* curves of both the PV module and the CoNH electrodes in the two-electrode cell (Supplementary materials Fig. S15b). These values are similar to the initial values obtained under the stability measurements corresponding to 6.53 mA cm^{-2} and 7.22 mA cm^{-2} for the 0 wt% GO/CoNHs and 12 wt % GO/CoNHs, respectively. The performance of solar-driven hydrogen generation in the electrolyzer was recorded under chopped light illumination. The fluctuation of the current density under illumination is caused by bubble formation on the surface, which affects the effective surface area [63]. These stability measurements demonstrated the superiority of the 12 wt% GO/CoNHs where ~78% of the initial current density remains and maintains stable after one hour compared to a more noticeable decay of the 0 wt% GO/CoNHs over time, representing a ~65% decay within one hour.

4. Conclusions and perspectives

We reported the design and fabrication of Co-based nanohybrids, using GO to enhance charge transport, thereby increasing the electrocatalytic activity and long-term stability of the electrodes. The resulting GO/CoNHs have interesting features including: (i) its formation from cost-effective earth-abundant transition metal oxides, (ii) a plausible pathway for *in situ* generation and self-repair of Co-based nanohybrids into cobalt chalcogenides, and (iii) remarkable long-term stability (up to 42 h in $\text{Na}_2\text{S}/\text{Na}_2\text{SO}_3$).

This approach is promising for eliminating dependence on platinum, whose performance decays dramatically within 35 min of operation (in $\text{Na}_2\text{S}/\text{Na}_2\text{SO}_3$), therefore increasing the viability of these emerging technologies. We observed that during long-term operation, the nanohybrids constituted of interconnected nanoparticles onto 1D nanostructures can follow a self-repairing/re-building of the electrocatalyst into 2D cobalt sulfide nanosheets endowing them with functional properties for stable and operational H_2 generation. Moreover, we have demonstrated that the as-prepared electrodes can also work effectively in an alkaline electrolyzer (1 M KOH) and in solar-driven water splitting devices. Superior performance may be achieved by increasing the electrocatalyst loading with complementary methods and/or using graphene with large amount of sp^2 conductive domains. Furthermore, employing our starting CoNHs as practical high surface area electrocatalysts and tuning their composition alloying with ternary elements might be another pathway to match the durability of these alternative electrodes in a wide pH range. The fundamental findings of exploiting GO and Co_3O_4 to obtain GO/CoNHs and the practical importance of using electrospinning as a nanostructuring approach defines the possibility of broadening the application of these alternative electrodes toward the fabrication of other renewable energy devices such as fuel cells, QDSCs and photocatalytic or PEC water splitting systems.

Acknowledgements

The authors are grateful to I. Ka for training and support provided for Raman measurements. We acknowledge J.G. Rivera, J.C. Abrego-Martinez and D. Benetti for helpful discussions on the electrochemical measurements. S.G.C., F.R. S.S. and A.C.T. acknowledge funding from the Natural Science and Engineering Research Council of Canada (NSERC) in the form of individual Discovery Grants. S.G.C. and F.R. acknowledge partial salary support and funding from the Canada Research Chairs program. F.R. is also grateful to the government of China for a Chang Jiang scholar short term award and to Sichuan province for a 1000 Talents Plan short-term award. H.Z. acknowledges the start funding support from Qingdao University and the funding from the Natural Science Foundation of Shandong Province (Grant No. ZR2018MB001). F.N.P. and G.S.S. are grateful to the UNESCO Chair MATECSS for a Postdoctoral Excellence Scholarship. F.N.P.

acknowledges funding from the UESTC and the National Natural Science Foundation of China (Grant No. 5171101224) and China Postdoctoral Science Foundation (Grant No. Y02006023607941).

Appendix A. Supplementary data

Supplementary material related to this article can be found, in the online version, at doi:<https://doi.org/10.1016/j.apcatb.2018.12.041>.

References

- [1] R. Lv, J.A. Robinson, R.E. Schaak, D. Sun, Y. Sun, T.E. Mallouk, M. Terrones, Transition metal dichalcogenides and beyond: synthesis, properties, and applications of single-and few-layer nanosheets, *Acc. Chem. Res.* 48 (2014) 56–64.
- [2] C. Yuan, H.B. Wu, Y. Xie, X.W.D. Lou, Mixed transition-metal oxides: design, synthesis, and energy-related applications, *Angew. Chem. Int. Ed.* 53 (2014) 1488–1504.
- [3] J. Wang, W. Cui, Q. Liu, Z. Xing, A.M. Asiri, X. Sun, Recent progress in cobalt-based heterogeneous catalysts for electrochemical water splitting, *Adv. Mater.* 28 (2016) 215–230.
- [4] M.S. Faber, S. Jin, Earth-abundant inorganic electrocatalysts and their nanostructures for energy conversion applications, *Energy Environ. Sci.* 7 (2014) 3519–3542.
- [5] F. Wang, H. Dong, J. Pan, J. Li, Q. Li, D. Xu, One-step electrochemical deposition of hierarchical CuS nanostructures on conductive substrates as robust, high-performance counter electrodes for quantum-dot-sensitized solar cells, *J. Phys. Chem. C* 118 (2014) 19589–19598.
- [6] Y. Tachibana, L. Vayssières, J.R. Durrant, Artificial photosynthesis for solar water-splitting, *Nat. Photon.* 6 (2012) 511–518.
- [7] R. von Hagen, H. Lorrmann, K.C. Möller, S. Mathur, Electrospun $\text{LiFe}_{1-y}\text{Mn}_y\text{PO}_4/\text{C}$ nanofiber composites as self-supporting cathodes in Li-ion batteries, *Adv. Energy Mater.* 2 (2012) 553–559.
- [8] Y. Wei, X. Ren, H. Ma, X. Sun, Y. Zhang, X. Kuang, T. Yan, H. Ju, D. Wu, Q. Wei, $\text{Co}_2\text{O}_4 \cdot 2\text{H}_2\text{O}$ derived Co_3O_4 nanorods array: a high-efficiency 1D electrocatalyst for alkaline oxygen evolution reaction, *Chem. Commun.* 54 (2018) 1533–1536.
- [9] M.S. Faber, K. Park, M. Cabán-Acevedo, P.K. Santra, S. Jin, Earth-abundant cobalt pyrite (CoS_2) thin film on glass as a robust, high-performance counter electrode for quantum-dot-sensitized solar cells, *J. Phys. Chem. Lett.* 4 (2013) 1843–1849.
- [10] J.S. Mondschein, J.F. Callejas, C.G. Read, J.Y. Chen, C.F. Holder, C.K. Badding, R.E. Schaak, Crystalline cobalt oxide films for sustained electrocatalytic oxygen evolution under strongly acidic conditions, *Chem. Mater.* 29 (2017) 950–957.
- [11] J. Yang, K. Walczak, E. Anzenberg, F.M. Toma, G. Yuan, J. Beeman, A. Schwartzberg, Y. Lin, M. Hettick, A. Javey, Efficient and sustained photoelectrochemical water oxidation by cobalt oxide/silicon photoanodes with nano-textured interfaces, *J. Am. Chem. Soc.* 136 (2014) 6191–6194.
- [12] M.S. Faber, R. Dziedzic, M.A. Lukowski, N.S. Kaiser, Q. Ding, S. Jin, High-performance electrocatalysis using metallic cobalt pyrite (CoS_2) micro-and nanostructures, *J. Am. Chem. Soc.* 136 (2014) 10053–10061.
- [13] H. Jin, J. Wang, D. Su, Z. Wei, Z. Pang, Y. Wang, In situ cobalt–cobalt oxide/N-doped carbon hybrids as superior bifunctional electrocatalysts for hydrogen and oxygen evolution, *J. Am. Chem. Soc.* 137 (2015) 2688–2694.
- [14] X. Yan, L. Tian, M. He, X. Chen, Three-dimensional crystalline/amorphous Co/ Co_3O_4 core/shell nanosheets as efficient electrocatalysts for the hydrogen evolution reaction, *Nano Lett.* 15 (2015) 6015–6021.
- [15] Y. Fu, C. Zhu, C. Liu, M. Zhang, H. Wang, W. Shi, H. Huang, Y. Liu, Z. Kang, CoMn-S/Cds nanocomposite for effective long wavelength visible-light-driven photocatalytic water splitting, *App. Cat. B: Environ.* 226 (2018) 295–302.
- [16] T. Hong, Z. Liu, X. Zheng, J. Zhang, L. Yan, Efficient photoelectrochemical water splitting over Co_3O_4 and $\text{Co}_3\text{O}_4/\text{Ag}$ composite structure, *App. Cat. B: Environ.* 202 (2017) 454–459.
- [17] H.K. Mulmudi, S.K. Batabyal, M. Rao, R.R. Prabhakar, N. Mathews, Y.M. Lam, S.G. Mhaisalkar, Solution processed transition metal sulfides: application as counter electrodes in dye sensitized solar cells (DSCs), *Phys. Chem. Chem. Phys.* 13 (2011) 19307–19309.
- [18] Y. Hu, D. Ye, B. Luo, H. Hu, X. Zhu, S. Wang, L. Li, S. Peng, L. Wang, A binder-free and free-standing cobalt sulfide@carbon nanotube cathode material for aluminum-ion batteries, *Adv. Mater.* 30 (2018) 1703824.
- [19] W. Guo, X. Zhang, R. Yu, M. Que, Z. Zhang, Z. Wang, Q. Hua, C. Wang, Z.L. Wang, C. Pan, CoS NWs/Au hybridized networks as efficient counter electrodes for flexible sensitized solar cells, *Adv. Energy Mater.* 5 (2015) 1500141.
- [20] S. Peng, L. Li, X. Han, W. Sun, M. Srinivasan, S.G. Mhaisalkar, F. Cheng, Q. Yan, J. Chen, S. Ramakrishna, Cobalt sulfide nanosheet/graphene/carbon nanotube nanocomposites as flexible electrodes for hydrogen evolution, *Angew. Chem. Int. Ed.* 53 (2014) 12594–12599.
- [21] J. Wang, D. Gao, G. Wang, S. Miao, H. Wu, J. Li, X. Bao, Cobalt nanoparticles encapsulated in nitrogen-doped carbon as a bifunctional catalyst for water electrolysis, *J. Mater. Chem. A* 2 (2014) 20067–20074.
- [22] H. Fei, J. Dong, M.J. Arellano-Jiménez, G. Ye, N.D. Kim, E.L. Samuel, Z. Peng, Z. Zhu, F. Qin, J. Bao, Atomic cobalt on nitrogen-doped graphene for hydrogen generation, *Nat. Commun.* 6 (2015) 8668.
- [23] G. Eda, G. Fanchini, M. Chhowalla, Large-area ultrathin films of reduced graphene oxide as a transparent and flexible electronic material, *Nat. Nanotechnol.* 3 (2008)

- 270–274.
- [24] X. Huang, X. Qi, F. Boey, H. Zhang, Graphene-based composites, *Chem. Soc. Rev.* 41 (2012) 666–686.
- [25] Y. Zheng, Y. Jiao, S.Z. Qiao, Engineering of carbon-based electrocatalysts for emerging energy conversion: from fundamentality to functionality, *Adv. Mater.* 27 (2015) 5372–5378.
- [26] L. Dai, D.W. Chang, J.B. Baek, W. Lu, Carbon nanomaterials for advanced energy conversion and storage, *Small* 8 (2012) 1130–1166.
- [27] F. Navarro-Pardo, H.G. Zhao, Z.M. Wang, F. Rosei, Structure/property relations in “giant” semiconductor nanocrystals: opportunities in photonics and electronics, *Acc. Chem. Res.* 51 (2018) 609–618.
- [28] X. Tong, X.-T. Kong, Y. Zhou, F. Navarro-Pardo, G.S. Selopal, S. Sun, A.O. Govorov, H. Zhao, Z.M. Wang, F. Rosei, Near-infrared, heavy metal-free colloidal “giant” core-shell quantum dots, *Adv. Energy Mater.* 8 (2018) 1701432.
- [29] X. Tong, Y. Zhou, L. Jin, K. Basu, R. Adhikari, G.S. Selopal, H. Zhao, S. Sun, A. Vomiero, Z.M. Wang, F. Rosei, Heavy metal-free, near-infrared colloidal quantum dots for efficient photoelectrochemical hydrogen generation, *Nano Energy* 31 (2017) 441–449.
- [30] G. Wang, X. Yang, F. Qian, J.Z. Zhang, Y. Li, Double-sided CdS and CdSe quantum dot co-sensitized ZnO nanowire arrays for photoelectrochemical hydrogen generation, *Nano Lett.* 10 (2010) 1088–1092.
- [31] J. Hensel, G. Wang, Y. Li, J.Z. Zhang, Synergistic effect of CdSe quantum dot sensitization and nitrogen doping of TiO₂ nanostructures for photoelectrochemical solar hydrogen generation, *Nano Lett.* 10 (2010) 478–483.
- [32] H. Zhao, F. Rosei, Colloidal quantum dots for solar technologies, *Chem* 3 (2017) 229–258.
- [33] J. Li, M.W. Hoffmann, H. Shen, C. Fabrega, J.D. Prades, T. Andreu, F. Hernandez-Ramirez, S. Mathur, Enhanced photoelectrochemical activity of an excitonic staircase in CdS@TiO₂ and CdS@anatase@rutile TiO₂ heterostructures, *J. Mater. Chem.* 22 (2012) 20472–20476.
- [34] J.-Y. Kim, Y.J. Jang, J. Park, J. Kim, J.S. Kang, D.Y. Chung, Y.-E. Sung, C. Lee, J.S. Lee, M.J. Ko, Highly loaded PbS/Mn-doped CdS quantum dots for dual application in solar-to-electrical and solar-to-chemical energy conversion, *App. Cat. B: Environ.* 227 (2018) 409–417.
- [35] X. Tong, X.T. Kong, C. Wang, Y. Zhou, F. Navarro-Pardo, D. Barba, D. Ma, S. Sun, A.O. Govorov, H. Zhao, Z.M. Wang, F. Rosei, Optoelectronic properties in near-infrared colloidal heterostructured pyramidal “giant” core/shell quantum dots, *Adv. Sci.* 5 (2018) 1800656.
- [36] J. Schneider, D.W. Bahnemann, Undesired role of sacrificial reagents in photocatalysis, *J. Phys. Chem. Lett.* 4 (2013) 3479–3483.
- [37] R. Adhikari, L. Jin, F. Navarro-Pardo, D. Benetti, B. AlOtaibi, S. Vanka, H. Zhao, Z. Mi, A. Vomiero, F. Rosei, High efficiency, Pt-free photoelectrochemical cells for solar hydrogen generation based on “giant” quantum dots, *Nano Energy* 27 (2016) 265–274.
- [38] F. Navarro-Pardo, L. Jin, R. Adhikari, X. Tong, D. Benetti, K. Basu, S. Vanka, H. Zhao, Z. Mi, S. Sun, V.M. Castano, A. Vomiero, F. Rosei, Nanofiber-supported CuS nanoplatelets as high efficiency counter electrodes for quantum dot-based photoelectrochemical hydrogen production, *Mater. Chem. Front.* 1 (2017) 65–72.
- [39] M. Antoniadou, S. Sfaelou, V. Dracopoulos, P. Lianos, Platinum-free photoelectrochemical water splitting, *Catal. Commun.* 43 (2014) 72–74.
- [40] M. Antoniadou, S. Sfaelou, P. Lianos, Quantum dot sensitized titania for photo-fuel-cell and for water splitting operation in the presence of sacrificial agents, *Chem. Eng. J.* 254 (2014) 245–251.
- [41] P.V. Kamat, Boosting the efficiency of quantum dot sensitized solar cells through modulation of interfacial charge transfer, *Acc. Chem. Res.* 45 (2012) 1906–1915.
- [42] P.C. Vesborg, B. Seger, I. Chorkendorff, Recent development in hydrogen evolution reaction catalysts and their practical implementation, *J. Phys. Chem. Lett.* 6 (2015) 951–957.
- [43] H. Chen, Z. Sun, S. Ye, D. Lu, P. Du, Molecular cobalt-salen complexes as novel cocatalysts for highly efficient photocatalytic hydrogen production over a CdS nanorod photosensitizer under visible light, *J. Mater. Chem. A* 3 (2015) 15729–15737.
- [44] J. Tian, Q. Liu, A.M. Asiri, X. Sun, Self-supported nanoporous cobalt phosphide nanowire arrays: an efficient 3D hydrogen-evolving cathode over the wide range of pH 0–14, *J. Am. Chem. Soc.* 136 (2014) 7587–7590.
- [45] W.S. Hummers Jr., R.E. Offeman, Preparation of graphitic oxide, *J. Am. Chem. Soc.* 80 (1958) 1339.
- [46] M.C. Biesinger, B.P. Payne, A.P. Grosvenor, L.W. Lau, A.R. Gerson, R.S.C. Smart, Resolving surface chemical states in XPS analysis of first row transition metals, oxides and hydroxides: Cr, Mn, Fe, Co and Ni, *Appl. Surf. Sci.* 257 (2011) 2717–2730.
- [47] J. Yang, H. Liu, W.N. Martens, R.L. Frost, Synthesis and characterization of cobalt hydroxide, cobalt oxyhydroxide, and cobalt oxide nanodisks, *J. Phys. Chem. C* 114 (2009) 111–119.
- [48] C. Vaz, D. Prabhakaran, E. Altman, V. Henrich, Experimental study of the interfacial cobalt oxide in Co₃O_{4/α} – Al₂O₃ (0001) epitaxial films, *Phys. Rev. B* 80 (2009) 155457.
- [49] D. Benetti, K.T. Dembele, J. Benavides, H. Zhao, S. Cloutier, I. Concina, A. Vomiero, F. Rosei, Functionalized multi-wall carbon nanotubes/TiO₂ composites as efficient photoanodes for dye sensitized solar cells, *J. Mater. Chem. C* 4 (2016) 3555–3562.
- [50] K.T. Dembele, G.S. Selopal, R. Milan, C. Trudeau, D. Benetti, A. Soudi, M.M. Natile, G. Sberveglieri, S. Cloutier, I. Concina, F. Rosei, A. Vomiero, Graphene below the percolation threshold in TiO₂ for dye-sensitized solar cells, *J. Mater. Chem. A* 3 (2015) 2580–2588.
- [51] K.T. Dembele, G.S. Selopal, C. Soldano, R. Nechache, J.C. Rimada, I. Concina, G. Sberveglieri, F. Rosei, A. Vomiero, Hybrid carbon nanotubes–TiO₂ photoanodes for high efficiency dye-sensitized solar cells, *J. Phys. Chem. C* 117 (2013) 14510–14517.
- [52] A. Mukherji, B. Seger, G.Q. Lu, L. Wang, Nitrogen doped Sr₂Ta₂O₇ coupled with graphene sheets as photocatalysts for increased photocatalytic hydrogen production, *ACS Nano* 5 (2011) 3483–3492.
- [53] K.K. Manga, Y. Zhou, Y. Yan, K.P. Loh, Multilayer hybrid films consisting of alternating graphene and titania nanosheets with ultrafast electron transfer and photoconversion properties, *Adv. Funct. Mater.* 19 (2009) 3638–3643.
- [54] M. Jahan, Z. Liu, K.P. Loh, A graphene oxide and copper-centered metal organic framework composite as a tri-functional catalyst for HER, OER, and ORR, *Adv. Funct. Mater.* 23 (2013) 5363–5372.
- [55] V. Hadjiev, M. Iliev, I. Vergilov, The Raman spectra of Co₃O₄, *J. Phys. C: Solid State Phys.* 21 (1988) L199.
- [56] A.C. Ferrari, J. Meyer, V. Scardaci, C. Casiraghi, M. Lazzeri, F. Mauri, S. Pisacane, D. Jiang, K. Novoselov, S. Roth, Raman spectrum of graphene and graphene layers, *Phys. Rev. Lett.* 97 (2006) 187401.
- [57] A. Akbari-Sharafab, S. Ezugwu, M.S. Ahmed, M.G. Cottam, G. Fanchini, Doping graphene thin films with metallic nanoparticles: experiment and theory, *Carbon* 95 (2015) 199–207.
- [58] K.P. Loh, Q. Bao, G. Eda, M. Chhowalla, Graphene oxide as a chemically tunable platform for optical applications, *Nat. Chem.* 2 (2010) 1015–1024.
- [59] L.G. Bloor, P.I. Molina, M.D. Symes, L. Cronin, Low pH electrolytic water splitting using earth-abundant metastable catalysts that self-assemble in situ, *J. Am. Chem. Soc.* 136 (2014) 3304–3311.
- [60] D.A. Lutterman, Y. Surendranath, D.G. Nocera, A self-healing oxygen-evolving catalyst, *J. Am. Chem. Soc.* 131 (2009) 3838–3839.
- [61] W. Liu, E. Hu, H. Jiang, Y. Xiang, Z. Weng, M. Li, Q. Fan, X. Yu, E.I. Altman, H. Wang, A highly active and stable hydrogen evolution catalyst based on pyrite-structured cobalt phosphosulfide, *Nat. Commun.* 7 (2016) 10771.
- [62] R.H. Coridan, A.C. Nielander, S.A. Francis, M.T. McDowell, V. Dix, S.M. Chatman, N.S. Lewis, Methods for comparing the performance of energy-conversion systems for use in solar fuels and solar electricity generation, *Energy Environ. Sci.* 8 (2015) 2886–2901.
- [63] J. Luo, J.-H. Im, M.T. Mayer, M. Schreier, M.K. Nazeeruddin, N.-G. Park, S.D. Tilley, H.J. Fan, M. Grätzel, Water photolysis at 12.3% efficiency via perovskite photovoltaics and earth-abundant catalysts, *Science* 345 (2014) 1593–1596.